

Controllable Low-Temperature Chemical Vapor Deposition Growth and Morphology Dependent Field Emission Property of SnO₂ Nanocone Arrays with Different Morphologies

Xiao-Bo Li,[†] Xue-Wen Wang,^{†,‡} Qiong Shen,[†] Jie Zheng,[§] Wei-Hua Liu,[§] Hua Zhao,[†] Fan Yang,[†] and He-Qing Yang^{*,†}

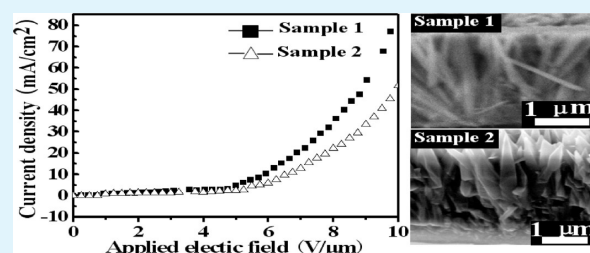
[†]Key Laboratory of Macromolecular Science of Shaanxi Province, School of Materials Science and Engineering, Shaanxi Normal University, Xi'an, 710062, China

[‡]i-Lab, Suzhou Institute of Nano-Tech and Nano-Bionics, Chinese Academy of Sciences, Suzhou, 215125, China

[§]School of Electronic and Information Engineering, Xi'an Jiaotong University, Xi'an, 710049, China

ABSTRACT: Vertically aligned SnO₂ nanocones with different morphologies have been directly grown on fluorine-doped tin oxide (FTO) glass substrates in a large area by heating a mixture of stannous chloride dihydrate (SnCl₂·2H₂O) and anhydrous zinc chloride (ZnCl₂) at 600 °C in air. Control over the SnO₂ nanocone arrays with different morphologies is achieved by adjusting the heat treatment time. The SnO₂ nanocones are single crystalline with the tetragonal structure. A single-layer SnO₂ nanoparticle film is first formed via the vapor–solid (VS) process due to the decentralization function of ZnCl₂ vapor, and the SnO₂ nanoparticles served as seeds and grew into nanocone arrays via the VS process. The sharp-tipped nanostructure formation may originate from a concentration gradient of reactant in the growth process. The as-obtained whiskerlike nanocone arrays exhibit enhanced field emission properties in comparison with typical nanoconelike structure arrays and other SnO₂ nanostructured materials reported previously, and the turn-on field and field-enhancement factor is 1.19 V/μm and 3110, respectively. The experimental result is consistent with the Utsumi's relative figure of merit for pillar-shaped emitters.

KEYWORDS: SnO₂ nanocone arrays, VS growth, field-emission



1. INTRODUCTION

Recently, one-dimensional (1D) and quasi-one-dimensional (quasi-1D) nanostructures, such as, nanowires, nanorods, nanotubes, and nanobelts, have attracted a great deal of attention owing to their interesting geometries, unique properties, and novel potential applications in nanoscale devices as interconnects or functional components.^{1,2} Tin dioxide (SnO₂) is a very important wide-band gap semiconductor ($E_g = 3.6$ eV at 300 K) and has been widely studied for a wide range of applications including optoelectronic devices, chemical gas sensors, dye-based solar cells, lithium batteries, and catalysts because of its excellent optical, electrical, and catalytic properties.^{3–5} Since the discovery of SnO₂ nanobelts in 2001,⁶ a variety of 1D and quasi-1D nanostructures of SnO₂ have been fabricated, including nanorods,⁷ nanowire,⁸ nanotubes,^{9,10} microcones,¹¹ nanoshuttles,¹² nanobelts,¹³ zigzag nanobelts,¹⁴ nanosprings,¹⁵ nanorings,¹⁵ nanorod arrays,¹⁶ nanowire arrays,¹⁷ nanobelt arrays,¹⁸ nanotube arrays,¹⁹ hierarchical nanostructures,^{20,21} and patterned nanoflowers.²² Field-effect transistors²³ and transparent thin-film transistors²⁴ have been obtained based on SnO₂ nanowires and were found to exhibit high-mobility values even at low nanowire coverage. Nanoribbons,²⁵ nanowires,²⁶ nanobelts,²⁷ nanorods,²⁸ nanowire network,²⁹ and nanotubes³⁰ of SnO₂ have been used to

fabricate gas sensors and exhibit higher sensitivity than SnO₂ powders. SnO₂ nanotube³¹ and nanorod arrays³² have been employed as anode materials for lithium ion batteries and exhibit high lithium storage capacity and excellent cycling performance.

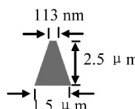
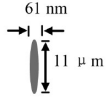
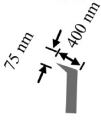
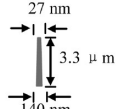
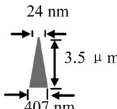
Field-emission (FE) is one of the main features of nanostructured materials and is of great commercial interest in displays and other electronic devices. The FE properties of films,³³ nanowires,⁸ nanobelts,¹⁸ nanoshuttles,¹² beaklike nanorods,³⁴ nanograss,³⁵ microcones,¹¹ hierarchical nanostructures,³⁶ patterned nanostructures³⁷ and nanoflowers,²² and nanorod arrays¹⁶ of SnO₂ have been studied, and the results show that the FE property is strongly related to the size and morphology of SnO₂ nanomaterials. The FE property of SnO₂ cone-shaped structure arrays has been reported.¹¹ However, the base of the cone-shaped structures is about a few micrometers in diameter, and the array orientation is poor. To our knowledge, morphology dependent field emission property of SnO₂ nanocone arrays has not been reported until now. In addition, the chemical vapor deposition (CVD) methods for

Received: December 7, 2012

Accepted: March 20, 2013

Published: March 20, 2013

Table 1. Method, Mechanism, and FE Property of Samples 1 and 2 as well as SnO₂ Cone-Shaped Structures Reported Previously

Microstructure	Microcone arrays	Nanoshuttles	Beaklike nanorods	Sample 1	Sample 2
Raw materials	Sn powder	Sn grains	Sn particles	SnCl ₂ ·2H ₂ O +7nCl ₂	SnCl ₂ ·2H ₂ O +7nCl ₂
Reaction temperature (°C)	850	900	1080	600	600
Atmosphere	Ar+Air	Ar+O ₂	Ar+O ₂	Air	Air
Growth mechanism	VS	VLS	VLS	VS	VS
Morphology					
Turn-on field (V/μm)	2.1 at 1 μA/cm ²	0.6 at 10 μA/cm ²	5.8 at 10 μA/cm ²	1.19 at 1 μA/cm ²	1.28 at 1 μA/cm ²
Field enhancement factor (β)	2280	3×10 ⁵	1402.9	3110	2947
Reference	(11)	(12)	(34)	This work	This work

the SnO₂ nanocones and nanoshuttles usually require high temperature (850–900 °C, Table 1). The CVD growth of vertically aligned SnO₂ nanocone arrays on conductive glass substrates has never been achieved until now.

On the basis of the volatility of the chlorides, we develop a low-temperature CVD process for the large area (1.2 cm × 1.2 cm) growth of highly oriented SnO₂ nanocone arrays with different morphologies. The SnO₂ nanocone arrays were directly grown on the fluorine-doped tin oxide (FTO) glass substrates by heating a mixture of stannous chloride dihydrate (SnCl₂·2H₂O) and anhydrous zinc chloride (ZnCl₂) to 600 °C in air. Control over the SnO₂ nanocones with different morphologies is achieved by adjusting the heat treatment time. The growth mechanism and FE properties of the SnO₂ nanocone arrays were investigated in detail, a possible mechanism is proposed, and the morphology dependent field-emission property is observed.

2. EXPERIMENTAL SECTION

SnCl₂·2H₂O and ZnCl₂ used were of analytical grade and were directly used as received without any further purification. Synthesis of SnO₂ nanocone arrays was carried out in a muffle furnace. The experiment setup is shown in Figure 1. In a typical experiment, 0.167 g of SnCl₂·2H₂O were mixed with 0.167 g of ZnCl₂ powders to form a

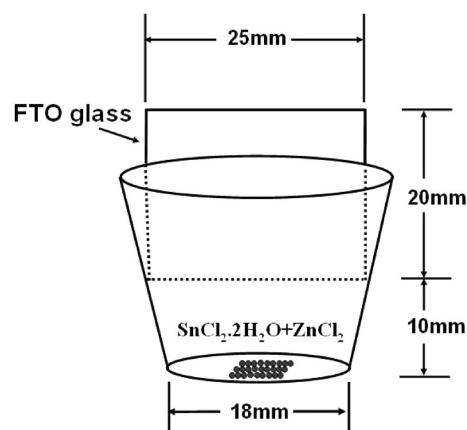


Figure 1. Schematic diagram of experimental apparatus for the synthesis of nanocone arrays.

mixture, and the mixture was put into a ceramic crucible. An FTO glass with dimensions of 2.5 cm × 2.0 cm was cleaned with deionized water and absolute ethanol in an ultrasound bath for 20 min, respectively. The FTO glass substrates were vertically inserted into the crucible, and the vertical distance between the Sn source and bottom of the FTO glass was about 10 mm. The crucible was placed at the center of the furnace. The furnace was heated up to 600 °C at a rate of 10 °C/min and kept at the temperature for different times. Then, the furnace was switched off and was cooled to room temperature naturally. Finally, a gray product was grown on the conductive glass substrate.

The as-prepared products were characterized and analyzed by X-ray diffraction (XRD), scanning electron microscopy (SEM), transmission electron microscopy (TEM), and X-ray photoelectron spectra (XPS). The XRD analysis was performed using a Rigaku DMX-IIIC X-ray diffractometer with Cu Kα₁ radiation (λ = 1.54 Å) at 40 kV and 30 mA. SEM images were obtained on a FEI Quanta 200 scanning electron microscope at an accelerating voltage of 20 kV and a JEOL JSM-6700F field emission scanning electron microscope at an accelerating voltage of 25 kV. An energy-dispersive X-ray spectroscopy (EDS) (EAX) facility attached to the Quanta 200 SEM was employed to analyze chemical composition. TEM images were obtained on a JEOL JEM-3010 transmission electron microscope at an accelerating voltage of 300 kV. Samples for TEM were prepared by dispersing the SnO₂ samples on a carbon-coated copper grid. XPS measurements were performed by using a Kratos Axis ultra X-ray photoelectron spectrometer with an excitation source of AlKα = 1486.7 eV.

3. RESULTS AND DISCUSSION

The products obtained for different heat treatment times were characterized by SEM and XRD, and the results are shown in Figures 2 and 4. Figure 2a–d shows typical SEM images of the products (sample 1) obtained by heating the mixture of SnCl₂·2H₂O and ZnCl₂ to 600 °C, closing up the furnace immediately and cooling down to room temperature naturally. The low magnification SEM images shown in Figure 2a and b represent the FTO glass substrate covered with large-scale nanocone arrays. The high magnification SEM image shown in Figure 2c shows clearly that the nanocones have flat quadrangular crystallographic planes on the top section, the typical tip width is distributed in the range 20–33 nm, and the averaged width is about 27 nm. A cross-sectional SEM image of the nanocone arrays is shown in Figure 2d, it clearly reveals that nanocones with lengths of 3–3.5 μm are oriented vertically with respect to the FTO glass substrate surface. The root

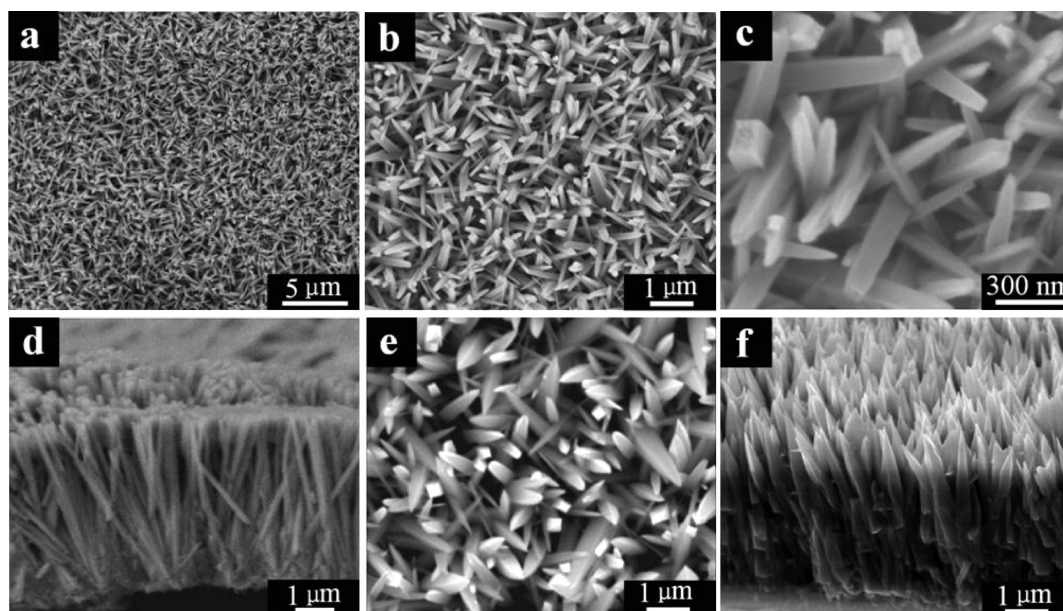


Figure 2. (a–c) Top-view SEM images of sample 1 at low and high magnifications, respectively. (d) Cross-sectional SEM image of sample 1. (e and f) Top-view and cross-sectional SEM image of sample 2, respectively.

widths of the nanocones are in the range of 120–160 nm, and the averaged width is about 140 nm. Figures 2e and f show the top-view and cross-sectional SEM images of the products (sample 2) obtained by the mixture of $\text{SnCl}_2 \cdot 2\text{H}_2\text{O}$ and ZnCl_2 at 600 °C for 60 min, respectively. The SEM observations indicate that nanocones with the lengths of 3.1–3.6 μm are directly grown on the FTO substrate. The tip and root widths of the nanocones are in the range of 17–37 and 332–440 nm, and their average value is 24 and 407 nm, respectively. The results suggest that nanocone arrays with different morphologies can be obtained by changing the heat treatment time. The EDS spectrum for sample 2 is shown in Figure 3, which

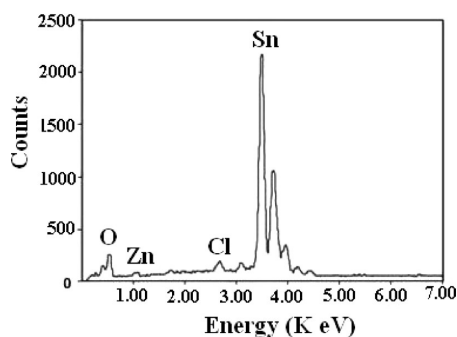


Figure 3. EDS spectrum of sample 2.

indicates that the nanocones consist of O, Sn, Zn, and Cl elements. The weight and atomic ratios of the elements are given in Table 2. The molar ratio of Sn:O was calculated to be 1:1.8, close to the stoichiometry of SnO_2 . The molar ratio of Zn:Cl was calculated to be 1:1.6, close to the stoichiometry of

Table 2. Chemical Compositions of Sample 2

element	Sn	O	Zn	Cl
weight ratio (%)	77.6	18.6	2.0	1.8
atomic ratio (%)	34.5	61.3	1.6	2.6

ZnCl_2 . Figures 4a and b show the XRD patterns of samples 1 and 2, respectively. All the diffraction peaks of the both samples

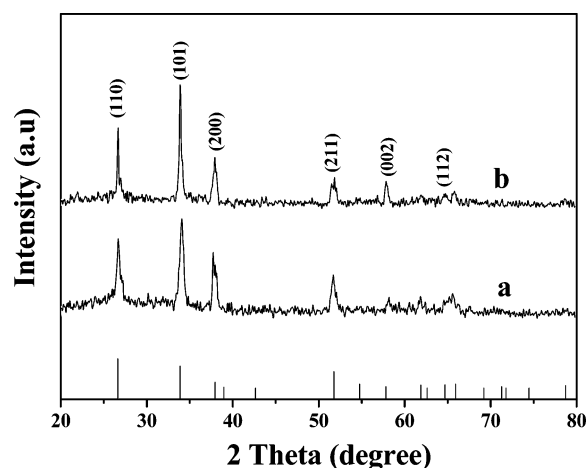


Figure 4. (a and b) XRD patterns of samples 1 and 2, respectively.

are readily indexed to the tetragonal phase of SnO_2 according to Joint Committee on Powder Diffraction Standards (JCPDS) card no. 41-1445. The SEM images and XRD patterns indicates the as-obtained samples 1 and 2 are SnO_2 nanocones with the tetragonal structure and a small quantity of ZnCl_2 coated on the surface of the SnO_2 nanocones.

Further structural details of the as-grown SnO_2 nanocones were investigated by TEM, and the results are shown in Figure 5. Figure 5a shows a typical TEM image of a single nanocone removed from the nanocone arrays of sample 1. TEM image reveals that the geometrical shape of the SnO_2 nanostructures is a cone. The diameters of the nanocones become lesser and lesser along its growth direction, and the tip diameter is 25 nm. Figures 5b and c show the selected area electron diffraction (SAED) pattern and high resolution TEM (HRTEM) image from the box in a, respectively. The SAED pattern shown in Figure 5b can be indexed as the $[-110]$ zone axis of single-

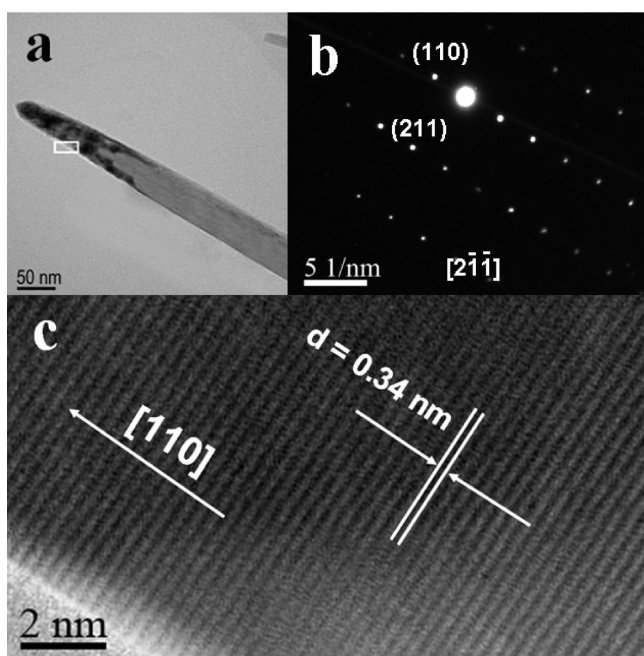


Figure 5. (a) Typical TEM image of a single nanocone removed from sample 1. (b) SAED pattern and (c) HRTEM image from the box in part a.

crystalline SnO_2 with the tetragonal structure. The lattice spacing of 0.34 nm can be observed clearly from the HRTEM image, which corresponds to the d spacing of (110) crystal planes of tetragonal phase SnO_2 . Both SAED and HRTEM confirm that the SnO_2 nanocones are single crystalline and grow along the direction perpendicular to (110) facets of SnO_2 with the tetragonal structures.

In order to understand the role of ZnCl_2 in the formation of SnO_2 nanocone arrays, $\text{SnCl}_2 \cdot 2\text{H}_2\text{O}$ was heated to 600 °C, stopped immediately, and allowed to cool down to room temperature naturally. The as-obtained products are characterized using SEM and EDS, and results are shown in Figure 6a and b. The SEM image and XRD pattern indicate that the products obtained without anhydrous ZnCl_2 are SnO_2 polycrystalline films with a tetragonal structure instead of SnO_2 nanocone arrays. Sample 2 was characterized by XPS, and the results are shown in Figure 7. The binding energies obtained in the XPS analysis were corrected for specimen charging through referencing the C 1s to 284.6 eV. The XPS spectra are shown in Figure 7, including (a) the survey spectrum, (b) Sn 3d, (c) O 1s, (d) Zn 2p, and (e) Cl 2p. In the full-range XPS survey spectrum, clear peaks for Sn, O, Zn, and Cl are observed. This result is in good agreement with the EDX analysis (Figure 3). The binding energy of Sn $3d_{5/2}$ and Sn $3d_{3/2}$ is identified at 486.3 and 494.7 eV, respectively (Figure 7b), which is derived from SnO_2 .^{38,39} Figure 7c depicts the O 1s line shape, which is significantly broader on the high-binding-energy side possibly due to the oxygen-deficient SnO_2 surfaces. The Gaussian fit of this peak leads to two separate peaks at 530.2 and 531.5 eV. The former is assigned to O^{2-} ions surrounded by fully coordinated Sn atoms, while the latter is attributed to the O^{2-} ions in oxygen deficient SnO_2 .⁴⁰ The binding energy of Zn $2p_{3/2}$ and Zn $2p_{1/2}$ is identified at 1022.2 and 1045.3 eV, respectively (Figure 7d).⁴¹ The binding energy of Cl $2p_{3/2}$ and Cl $2p_{1/2}$ is identified at 198.9 and 200.3 eV, respectively.⁴² The Zn and Cl peaks might come from ZnCl_2

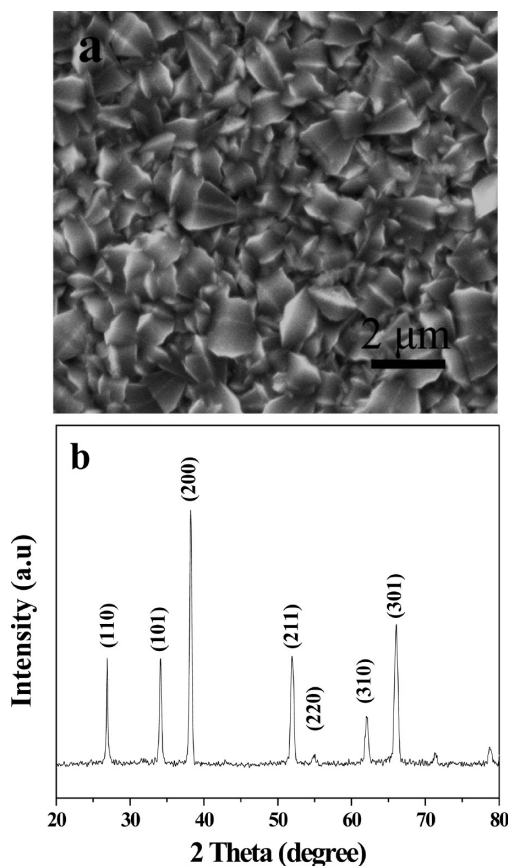


Figure 6. (a) SEM image and (b) XRD pattern of the products obtained via heating $\text{SnCl}_2 \cdot 2\text{H}_2\text{O}$ powders to 600 °C in air.

absorbed on the surface of the SnO_2 nanocones. Therefore, the ZnCl_2 plays an important role in the formation of SnO_2 nanocone arrays, but did not react with H_2O .

In order to further understand the growth of SnO_2 nanocone arrays, the products obtained by heating the mixture of ZnCl_2 and $\text{SnCl}_2 \cdot 2\text{H}_2\text{O}$ to 400 °C were characterized using SEM and EDS, and the results are shown in Figure 8a and b. The SEM observation reveals that the products synthesized by heating the mixture of $\text{SnCl}_2 \cdot 2\text{H}_2\text{O}$ and ZnCl_2 to 400 °C are a single-layer nanoparticle film. The size of the nanoparticles is in the range of 26–87 nm. In the EDS spectrum shown in Figure 8b, Sn, O, and Si elements were marked. The Si-related peak is due to the presence of conductive glass substrate. So, the nanoparticles consist of O and Sn elements. After deleting SiO_2 , the molar ratio of Sn:O was calculated to be 1:2, close to the stoichiometry of SnO_2 . Moreover, we found that the as-obtained products are inhomogeneous. In addition to large-scale SnO_2 nanocone arrays, nanorod arrays were also observed on bottom region of the FTO glass substrate. The distributing schematic diagram of the SnO_2 nanostructures in different geometrical morphologies grown on the FTO glass substrate is shown in Figure 9a. Figure 9b and c show typical SEM images from regions I and II in part a, respectively. The SEM observations indicate that the products grown in region I are nanorod arrays and the products grown in region II are arrays of nanorods and nanocones. The appropriate growth height is in the range of 16–30 nm for SnO_2 nanocone arrays. The above results suggest that ZnCl_2 powder only be vaporized in the reaction system and did not react with H_2O . However, it plays a vital role in the formation of single-layer SnO_2

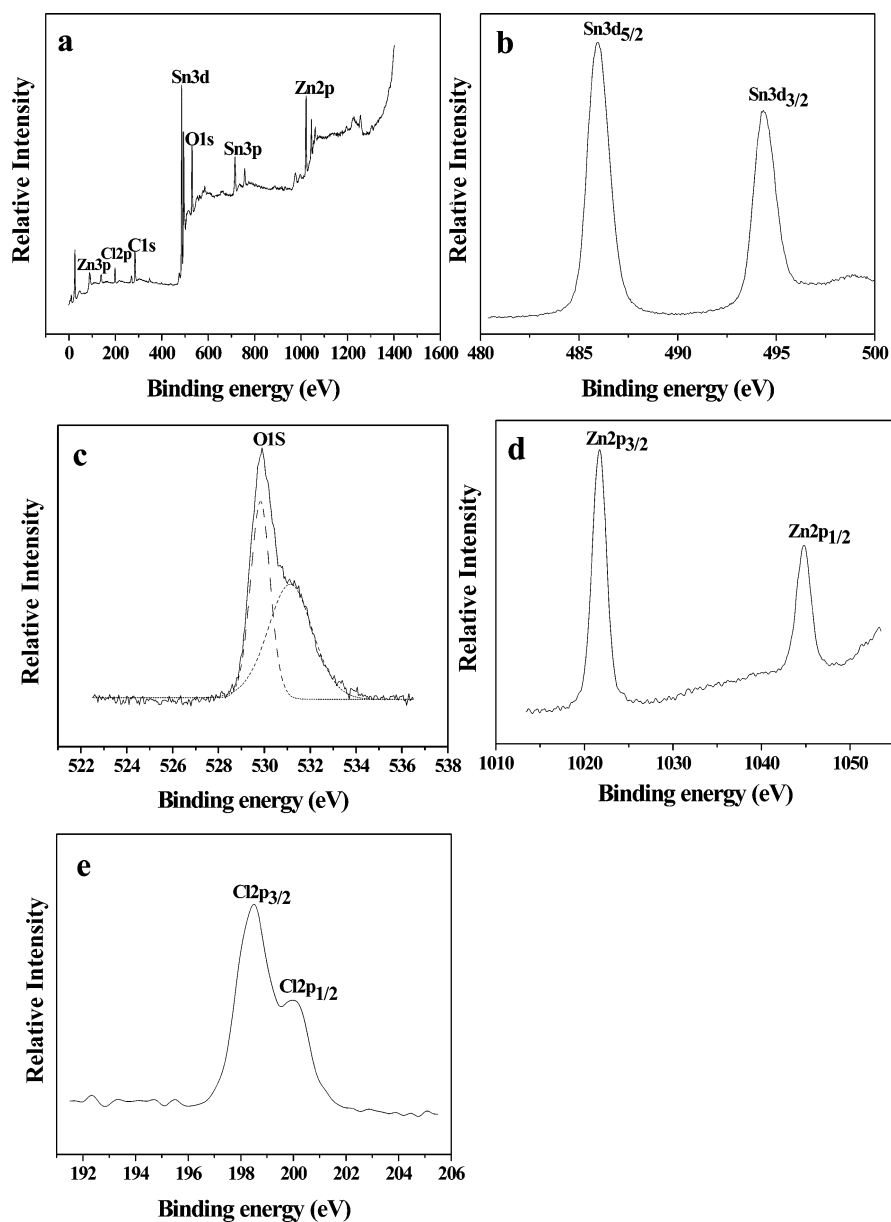
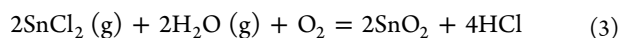
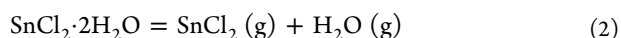


Figure 7. (a) Full-range XPS scan of samples; (b) Sn 3d scan; (c) O 1s scan; (d) Zn 2p scan; and (e) Cl 2p scan.

nanoparticle films and nanocone arrays. Therefore, it is reasonable to conclude that ZnCl_2 may serve as a dispersant to disperse the as-deposited SnO_2 in the CVD system.

In the CVD system, no catalyst was employed, and no liquid droplet was found at the end of the nanocones. Therefore, we consider that the growth of the SnO_2 nanocones is controlled by the vapor–solid (VS) process. The ZnCl_2 powder was vaporized to form ZnCl_2 vapor during the heat treatment, at the same time, $\text{SnCl}_2 \cdot 2\text{H}_2\text{O}$ powder was decomposed into SnCl_2 and H_2O vapor. The SnCl_2 vapor reacted with H_2O vapor and O_2 to form SnO_2 in the reaction chamber. The chemical reactions to form SnO_2 can be formulated as follow:



On the basis of the investigations described above, a possible mechanism to form SnO_2 nanocone arrays was proposed. As illustrated in Figure 10, when the mixture of ZnCl_2 and $\text{SnCl}_2 \cdot 2\text{H}_2\text{O}$ is heated to 400°C , the SnO_2 vapor formed by reaction 3 deposited directly on the surface of the FTO glass substrate and formed SnO_2 crystalline nuclei. The ZnCl_2 vapor formed by reaction 1 dispersed SnO_2 vapor and SnO_2 crystalline nuclei to form a single-layer SnO_2 nanoparticle film on the FTO glass substrate (step b). The SnO_2 nanoparticles served as seeds for subsequent growth. As the temperature increased to 600°C , the single layer SnO_2 nanoparticle films grew into nanocone arrays via the VS process (step c–d). The sharp-tipped SnO_2 nanocone formation may originate from a concentration gradient of reactant in the growth process.^{43,44} In the initial growth stage, SnO_2 vapor formed via reaction 3 is adequate, and the SnO_2 nanorods grow out from the SnO_2 nanoparticles. The Sn source will decrease with the experiment processing. The deficient SnO_2 vapor makes some growth steps remain on the nanorods.

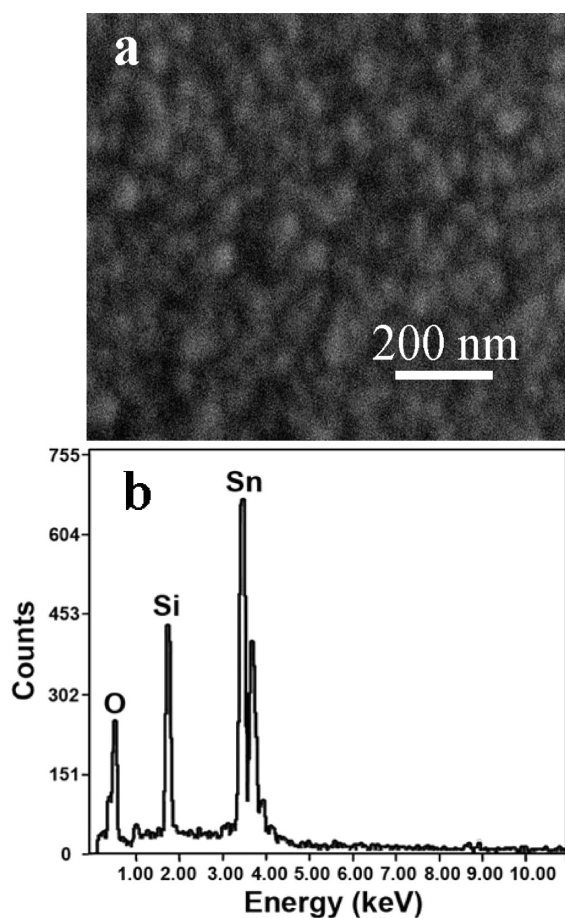


Figure 8. (a) SEM image and (b) EDS spectrum of the products synthesized by heating the mixture of ZnCl_2 and $\text{SnCl}_2 \cdot 2\text{H}_2\text{O}$ to 400 °C in air, closing up the furnace immediately and cooling down to room temperature naturally.

Then, the nanorods become smaller and smaller in the growth process; in the end, they grow into conelike nanostructures. However, when the heat treatment time at 600 °C is increased to 60 min, the base of the SnO_2 nanocones grew continuously via an oriented attachment process.^{45–47} The mean width of the cones on the root is increased from 140 to 407 nm, the average tip width is decreased from 27 to 24 nm, and thus the conelike structure becomes more distinct. When the growth height is in the range 10–14 mm, SnO_2 vapor formed via reaction 3 can meet the growth of SnO_2 nanorods, as a result, forming nanorod arrays. As the growth height is in the range 14–16 mm, SnO_2 vapor can meet the growth of SnO_2 nanorods partially, and thus, arrays of nanorods and nanocones are obtained. When the growth height is in the range 16–30 mm, The SnO_2 vapor could not meet for the growth of SnO_2 nanorods, a concentration gradient of SnO_2 vapor can be produced in the growth process, and thus the nanocone arrays are formed.

The FE measurements of the as-grown SnO_2 nanocone arrays were carried out in a vacuum chamber at a pressure of 3×10^{-5} Pa at room temperature. The SnO_2 nanocone arrays grown on the FTO glass substrate with an area of 0.5 cm \times 0.5 cm were used as a cathode, and an indium-doped tin oxide (ITO) conductive glass plate was used as an anode. The distance between the anode and the cathode is fixed at about 200 μm . The schematic diagram of the FE measurement system

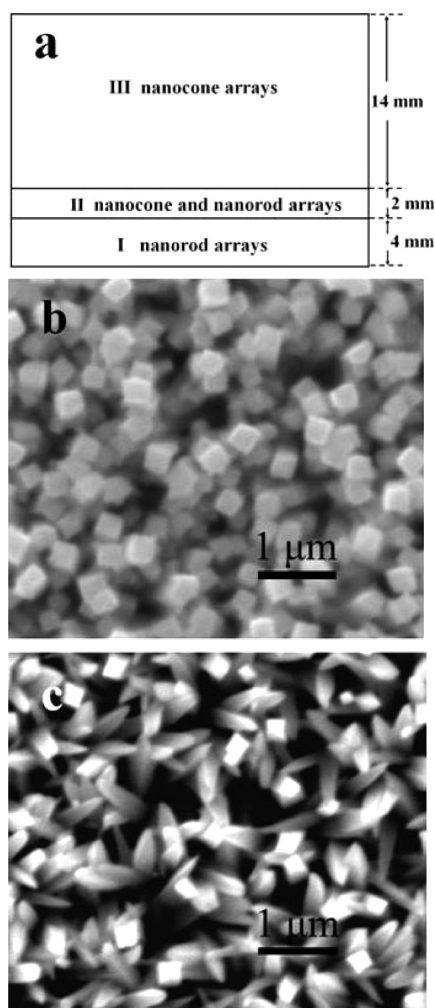


Figure 9. (a) Distributing schematic diagram of the SnO_2 nanostructures in different geometrical morphologies grown on the FTO glass substrate. (b and c) Typical SEM images from regions I and II in part a, respectively.

is shown in Figure 11a. The applied voltage was increased from 0 to 2.0 kV with a step of 50 V. Figure 11b shows the emission current density as a function of the applied electrical field for samples 1 and 2. The turn-on field (defined as the electric field required to generate a current density of $1 \mu\text{A}/\text{cm}^2$) for samples 1 and 2 is 1.19 and 1.28 $\text{V}/\mu\text{m}$, respectively. These values of turn-on field and data from other SnO_2 cone-shaped structures reported previously were summarized in Table 1. It was found that the value of turn-on field of the sample 1 is lower than that of sample 2 and is lower than the data from bealike nanorods³⁴ or microcones¹¹ reported previously. A lowered FE potential barrier arising from the field enhancement at the tip may lead to a decrease of the required field.³⁵ According to the classical Fowler–Nordheim (FN) theory for field emission, the relation between the emission current density (J) and the applied field ($E = V/d$) can be expressed by the following FN equation.⁴⁸

$$J = (A\beta^2 E^2 / \phi) \exp(-B\phi^{3/2} / \beta E) \quad (4)$$

Where J is the current density (A/m^2), E is the applied electric field ($\text{V}/\mu\text{m}$), ϕ is the work function of the emitting material (eV), and β is the field-enhancement factor, which is strongly related to the emitter geometry, crystal structure, and spatial distribution of the emitting centers. A and B are constants with

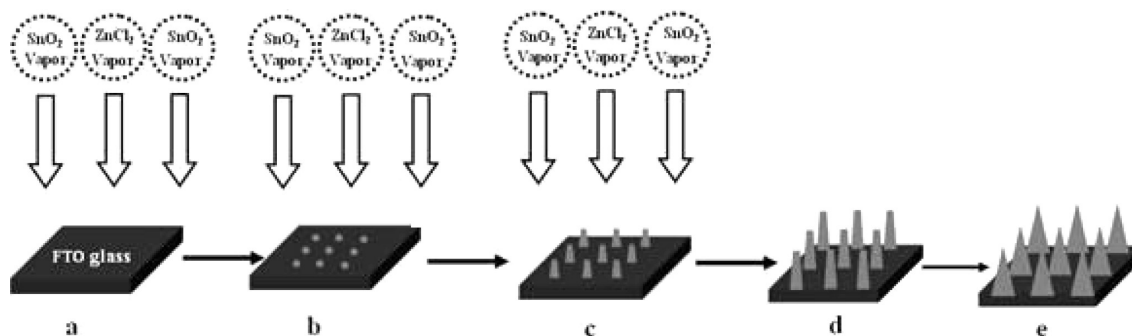


Figure 10. Schematic diagram of the growth mechanism of SnO₂ nanocone arrays.

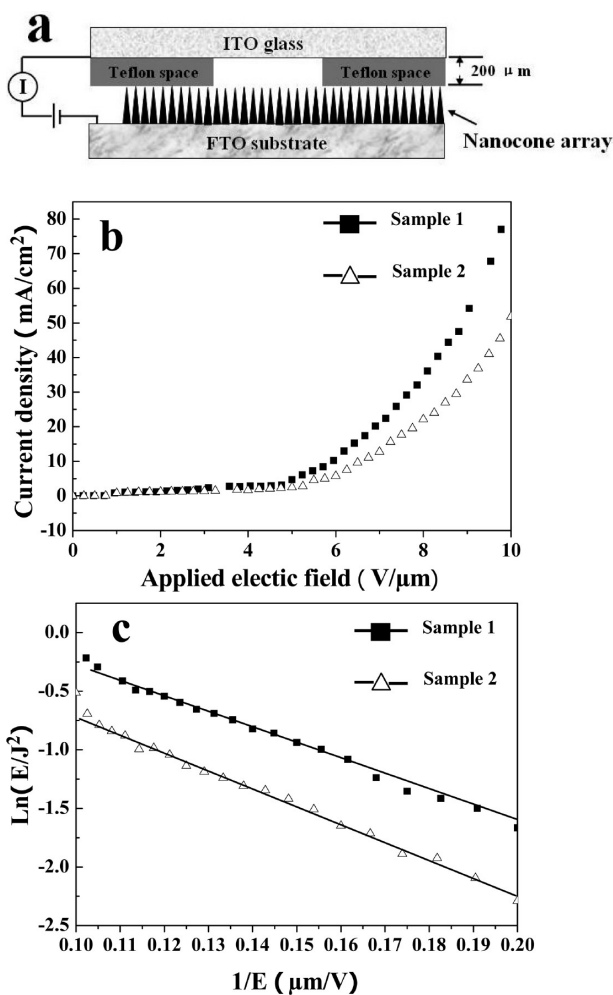


Figure 11. (a) Schematic illustration of the FE measurement system. (b) FE current density vs electric field (J – E) for samples 1 and 2. (c) Corresponding FN plots of samples 1 and 2.

$A = 1.56 \times 10^{-10}$ (A eV/V²) and $B = 6.83 \times 10^3$ (V/μm eV^{-3/2}), respectively. Figure 11c shows the plots of $\ln(J/E^2)$ versus $1/E$, i.e., the FN plot, for samples 1 and 2. By plotting $\ln(J/E^2)$ against $1/E$, a straight line was obtained for samples 1 and 2. The linear behavior of the plot indicates that the field emission behavior of the as-obtained SnO₂ nanocone arrays may have deviated from the FN description slightly. The field enhancement factor β is calculated from the slope ($-B\phi^{3/2}/\beta$) of the FN plot. By assuming the work function of $\phi = 4.5$ eV for SnO₂,⁴⁹ the calculated β value is about 3110 and 2947 for samples 1 and 2, respectively. All the β values of SnO₂ cone-

shaped structures reported until now were shown in Table 1. We can clearly observe that the β value of the sample 1 is larger than that of sample 2 and is much larger than the data from beaklike nanorods³⁴ and microcones¹¹ reported previously. The comparative result indicates that the as-synthesized SnO₂ whiskerlike nanocone arrays possess excellent FE performance and are a promising candidate in future FE device applications.

In order to check the validity of the obtained high β value in the present case, an independent estimate for the enhancement factor based on geometrical conditions of the emitter structure was performed. According to Zhao et al.,⁵⁰ the enhancement factor from array emitters can be defined as

$$\beta \approx 1 + s(d/r) \quad (5)$$

Where s is the screening effect parameter, d and r are anode to cathode spacing and radius of curvature for the emitter, respectively. For samples 1 and 2 shown in Figures 1a–d and e and f, the averaged r is taken to be 14 and 12 nm, respectively, and d is 200 μm in our measurement setup. Thus, by assuming $s = 1$ (i.e., no field screening effect from the presence of neighboring emitters), the enhancement factors were estimated to be 14 285 and 16 666 for samples 1 and 2, respectively. The β values derived from the slope of the FN plot and eq 5 suggest the corresponding screening effect parameters are about 0.22 and 0.18 for samples 1 and 2, respectively. The result is consistent with Utsumi's relative figure of merit for pillar-shape emitters. Utsumi⁵¹ evaluated four kinds of commonly used field emission tip shapes as shown in Figure 12 and concluded that

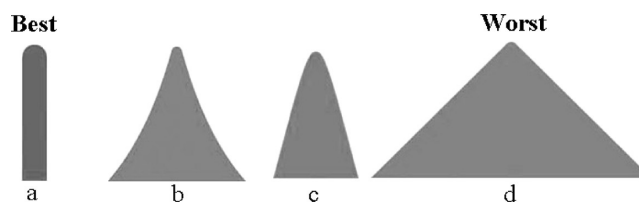


Figure 12. Classification and ranking of tip-shapes proposed by Utsumi⁵¹ From best to worst: (a) rounded whisker which is ideal, (b) sharpened pyramid, (c) hemispheroidal, and (d) pyramidal.

the best field emission tip should be whiskerlike followed by the sharpened pyramid, hemispheroidal, and pyramidal shapes. Indeed, nanocones of sample 1 are whiskerlike as shown in Figure 12. Therefore, the excellent FE performance of the as-grown SnO₂ whiskerlike nanocone arrays is attributed to the small radius of curvature for cone emitter,^{52–54} the good vertical alignment on the substrates,^{52–54} and the whiskerlike structures.⁵⁵

4. CONCLUSIONS

In summary, the whiskerlike and typical SnO₂ nanocone arrays were grown on the FTO glass substrates by a very simple low temperature chemical vapor deposition process, and their controllable growth is achieved by adjusting the heat treatment time. The function of the ZnCl₂ added in the raw materials has been studied, and a possible mechanism is proposed to account for the growth of the SnO₂ nanocone arrays. This simple and mild approach to fabricate SnO₂ nanocone arrays can be easily scaled up and potentially extended to the synthesis of other oxide nanocone arrays. Compared with typical nanoconelike structure arrays and other SnO₂ nanostructured materials reported previously, the whiskerlike nanocone arrays exhibit enhanced field emission property and are promising materials for fabricating efficient emitters in the application of display devices and vacuum electronics.

AUTHOR INFORMATION

Corresponding Author

*Fax: 0086-29-81530702. E-mail: hqyang@snnu.edu.cn (H.-Q.Y.).

Notes

The authors declare no competing financial interest.

ACKNOWLEDGMENTS

This work was supported by the National Natural Science Foundation of China (Grant No. 21073116), the Natural Science Foundation of Shaanxi Province (Grant No. 2010JM2011), and the Fundamental Research Funds for the Central Universities (Grant No. GK201101003).

REFERENCES

- (1) Mathur, S.; Barth, S.; Shen, H.; Pyun, J. C.; Werner, U. *Small* **2005**, *1*, 713.
- (2) Choe, Y. S. *Sens. Actuators, B* **2001**, *77*, 200–208.
- (3) Liu, R.; Yang, S. C.; Wang, F.; Lu, X. G.; Yang, Z. M.; Ding, B. J. *ACS Appl. Mater. Interfaces* **2012**, *4*, 1537–1542.
- (4) Chen, Y. J.; Zhu, C. L.; Cao, M. S.; Wang, T. H. *Nanotechnology* **2007**, *18*, 285502.
- (5) Wen, Z. H.; Wang, G.; Lu, W.; Wang, Q.; Zhang, Q.; Li, J. H. *Cryst. Growth Des.* **2007**, *7*, 1722–1725.
- (6) Pan, Z. W.; Dai, Z. R.; Wang, Z. L. *Science* **2001**, *291*, 1947–1949.
- (7) Cheng, B.; Russell, J. M.; Shi, Zhang, L.; Samulski, E. T. *J. Am. Chem. Soc.* **2004**, *126*, 5972–5973.
- (8) Li, L. J.; Zong, F. J.; Cui, X. D.; Ma, H. L.; Wu, X. H.; Zhang, Q. D.; Wang, Y. L.; Yang, F.; Zhao, J. Z. *Mater. Lett.* **2007**, *61*, 4152–4155.
- (9) Shi, L.; Lin, H. L. *Langmuir* **2011**, *27*, 3977–3981.
- (10) Wang, Y.; Lee, J. M.; Zeng, H. C. *Chem. Mater.* **2005**, *17*, 3899–3903.
- (11) Ma, L. A.; Guo, T. L. *Phys. B* **2008**, *403*, 3410–3413.
- (12) Li, J. J.; Chen, M. M.; Tian, S. B.; Jin, A. Z.; Xia, X. X.; Gu, C. Z. *Nanotechnology* **2011**, *22*, 505601.
- (13) Kumar, S.; Hesketh, P. J. *Nanotechnology* **2010**, *21*, 325501.
- (14) Duan, J. H.; Yang, S. G.; Liu, H. W.; Gong, J. F.; Huang, H. B.; Zhao, X. N.; Zhang, R.; Du, Y. W. *J. Am. Chem. Soc.* **2005**, *127*, 6180–6181.
- (15) Yang, R. S.; Wang, Z. L. *J. Am. Chem. Soc.* **2006**, *128*, 1466–1467.
- (16) Wang, X. W.; Liu, W. H.; Yang, H. Q.; Li, X. B.; Li, N.; Shi, R. Y.; Zhao, H.; Yu, J. *Acta Mater.* **2011**, *59*, 1291–1299.
- (17) Mazeina, L.; Picard, Y. N.; Caldwell, J. D.; Glaser, E. R.; Prokes, S. M. *J. Cryst. Growth* **2009**, *311*, 3158–3162.
- (18) Chen, Y. J.; Li, Q. H.; Liang, Y. X.; Wang, T. H. *Appl. Phys. Lett.* **2004**, *85*, 5682–5684.
- (19) Zhu, W.; Wang, W. Z.; Xu, H. L.; Shi, J. L. *Mater. Chem. Phys.* **2006**, *99*, 127–130.
- (20) Sun, S. H.; Meng, G. W.; Zhang, G. X.; Masse, J. P.; Zhang, L. D. *Chem.—Eur. J.* **2007**, *13*, 9087–9092.
- (21) Liu, J.; Chen, X. L.; Wang, W. J.; Song, B.; Huang, Q. S. *Cryst. Growth Des.* **2009**, *9*, 1757–1761.
- (22) Zhang, Y. S.; Yu, K.; Li, G. D.; Peng, D. Y.; Zhang, Q. X.; Xu, F.; Bai, W.; Ouyang, S. X.; Zhu, Z. Q. *Mater. Lett.* **2006**, *60*, 3109–3112.
- (23) Cheng, Y.; Xiong, P. *Nano Lett.* **2008**, *8*, 4179–4184.
- (24) Dattoli, E. N.; Wan, Q.; Guo, W.; Chen, Y. B.; Pan, X. Q.; Wei, L. *Nano Lett.* **2007**, *7*, 2463–2469.
- (25) Law, M.; Kind, H.; Messer, B.; Kim, F.; Yang, P. D. *Angew. Chem., Int. Ed.* **2002**, *41*, 2405–2408.
- (26) Wang, B.; Zhu, L. F.; Yang, Y. H.; Xu, N. S.; Yang, G. W. *J. Phys. Chem. C* **2008**, *112*, 6643–6647.
- (27) Calestani, D.; Lazzarini, L.; Salviati, G.; Zha, M. *Cryst. Res. Technol.* **2005**, *40*, 937–941.
- (28) Xue, X. Y.; Chen, Z. H.; Ma, C. H.; Xing, L. L.; Chen, Y. J.; Wang, Y. G.; Wang, T. H. *J. Phys. Chem. C* **2010**, *114*, 3968–3972.
- (29) Kolmakov, A.; Klenov, D. O.; Lilach, Y.; Stemmer, S.; Moskovits, M. *Nano Lett.* **2005**, *5*, 667–673.
- (30) Wang, G. X.; Park, J. S.; Park, M. S.; Gou, X. L. *Sens. Actuators, B* **2008**, *131*, 313–317.
- (31) Wang, J. Z.; Du, N.; Zhang, H.; Yu, J. X.; Yang, D. R. *J. Phys. Chem. C* **2011**, *115*, 11302–11305.
- (32) Liu, J. P.; Li, Y. Y.; Huang, X. T.; Ding, R. M.; Hu, Y. Y.; Jiang, J.; Liao, L. J. *Mater. Chem.* **2009**, *19*, 1859–1864.
- (33) Baranauskas, V.; Fontana, M.; Guo, Z. L. *Sens. Actuators, B* **2005**, *107*, 474–478.
- (34) He, J. H.; Wu, T. H.; Hsin, C. L.; Li, K. M.; Chen, L. J.; Chueh, Y. L.; Chou, L. J.; Wang, Z. L. *Small* **2006**, *2*, 116–120.
- (35) Wang, B.; Yang, Y. H.; Wang, C. X.; Xu, N. S.; Yanga, G. W. *J. Appl. Phys.* **2005**, *98*, 124303.
- (36) Wang, Q. Y.; Yu, K.; Xu, F. *Solid State Commun.* **2007**, *143*, 260–263.
- (37) Zhang, Y. S.; Yu, K.; Li, G. D.; Peng, D. Y.; Zhang, Q. X.; Hu, H. M.; Xu, F.; Bai, W.; Ouyang, S. X.; Zhu, Z. Q. *Appl. Surf. Sci.* **2006**, *253*, 792–796.
- (38) Renard, L.; Babot, O.; Saadaoui, H.; Fuess, H.; Brotz, J.; Gurlo, A.; Arveux, E.; Klein, A.; Toupance, T. *Nanoscale* **2012**, *4*, 6806.
- (39) Ahn, H. J.; Choi, H. C.; Park, K. W.; Kim, S. B.; Sung, Y. E. *J. Phys. Chem. B* **2004**, *108*, 9815–9820.
- (40) Ghosh, K.; Kumar, M.; Wang, H. F.; Maruyama, T.; Ando, Y. *Langmuir* **2010**, *26*, 5527–5533.
- (41) Zheng, L. R.; Zheng, Y. H.; Chen, C. Q.; Zhan, Y. Y.; Lin, X. Y.; Zheng, Q.; Wei, K. M.; Zhu, J. F. *Inorg. Chem.* **2009**, *48*, 1819–1825.
- (42) Yang, H. Q.; Shi, R. Y.; Yu, J.; Liu, R. N.; Zhang, R. G.; Zhao, H.; Zhang, L. H.; Zheng, H. R. *J. Phys. Chem. C* **2009**, *113*, 21548–21554.
- (43) Zhang, Z. X.; Yuan, H. J.; Zhou, J. J.; Liu, D. F.; Luo, S. D.; Miao, Y. M. *J. Phys. Chem. B* **2006**, *110*, 8566–8569.
- (44) Ma, J. H.; Yang, H. Q.; Song, Y. Z.; Li, L.; Xie, X. L.; Liu, R. N.; Wang, L. F. *Sci. China, Ser. E* **2009**, *52*, 1264–1272.
- (45) Yang, H. G.; Zeng, H. C. *Angew. Chem., Int. Ed.* **2004**, *43*, 5930–5933.
- (46) Pacholski, C.; Kornowski, A.; Weller, H. *Angew. Chem., Int. Ed.* **2002**, *41*, 1188–1191.
- (47) Li, L.; Yang, H. Q.; Qi, G. C.; Ma, J. H.; Xie, X. L.; Zhao, H.; Gao, F. *Chem. Phys. Lett.* **2008**, *455*, 93–97.
- (48) Ma, L. A.; Ye, Y.; Hu, L. Q.; Zheng, K. L.; Guo, T. L. *Phys. E* **2008**, *40*, 3127–3130.
- (49) Szuber, J.; Czempik, G.; Larciprete, R.; Adamowicz, B. *Sens. Actuators, B* **2000**, *70*, 177–181.
- (50) Zhao, Q.; Zhang, H. Z.; Zhu, Y. W.; Feng, S. Q.; Sun, X. C. *Appl. Phys. Lett.* **2005**, *86*, 203115.
- (51) Utsumi, T. *IEEE Trans. Electron Devices* **1991**, *38*, 2276–2283.

(52) Zhang, Z. S.; Huang, J. Y.; He, H. P.; Lin, S. S.; Tang, H. P.; Lu, H. M.; Ye, Z. Z. *Solid-State Electron.* **2009**, *53*, 578–583.

(53) Fang, X. S.; Bando, Y. S.; Gautam, U. K.; Ye, C. H.; Golberg, D. *J. Mater. Chem.* **2008**, *18*, 509–522.

(54) Yang, F.; Liu, W. H.; Wang, X. W.; Zheng, J.; Shi, R. Y.; Zhao, H.; Yang, H. Q. *ACS Appl. Mater. Interfaces* **2012**, *4*, 3852–3859.

(55) Milne, W. I.; Teo, K. B. K.; Amaratung, G. A. J.; Legagneux, P.; Gangloff, L.; Schnell, J. P.; Semet, V.; Binhc, V. T.; Groeningd, O. J. *Mater. Chem.* **2004**, *14*, 933–943.